Optimized Analytical Computation of Partial Elements Using a Retarded Taylor Series Expansion

Daniele Romano, Ivana Kovacevic-Badstuebner, *Senior Member, IEEE*, Ulrike Grossner, *Member, IEEE*, and Giulio Antonini, *Senior Member, IEEE*

***Abstract*—The aim of this article is to efficiently and accurately calculate the integrals of the full-wave (FW) partial element equivalent circuit (PEEC) method. The accuracy of the analytical formulas calculated by the standard precision can be compromised when using nonuniform mesh to properly model the high-frequency effects. The numerical errors can be avoided by using a high-precision arithmetic, i.e., higher number of digits, however, at the expense of significantly higher computation time. This article presents an analytical approach for calculating the FW-PEEC interaction integrals of two elementary volumes/surfaces based on the Taylor expansion, which allows a high computational speed preserving the accuracy with a relative error of less than 0.1%. The proposed solution is verified compared to the high-precision arithmetic and the standard Gaussian integration for two examples of strip lines. Moreover, it is shown that the accuracy of FW-PEEC integrals can affect the convergence of an iterative PEEC matrix solver.**

***Index Terms*—Adaptive integration, electric field, integral equations, numerical integration, partial element equivalent circuit (PEEC) method, Taylor series expansion.**

I. Introduction

ELECTROMAGNETICS modeling has received increasing interest in recent decades due to its ability to predict the electromagnetic performance of an electronic system in an early design phase much before the realization of a physical prototype. For this purpose, consequently, the numerical solution of Maxwell's equations has acquired increasing importance and has become a powerful tool for designers. Many methods have developed over the years, such as the finite-difference time-domain technique [1], the finite-element method [2], the method of moments [3], and the partial element equivalent circuit (PEEC) method [4], [5], [6], [7].

Nowadays, the most challenging objective is the development of a method that is accurate from the very low frequencies, including dc, to the highest frequencies that can easily reach the tens of gigahertz. Among the methods listed above, the PEEC method is different as it can transform an electromagnetic problem into a circuit model, in which the circuit parameters model the dissipative phenomena and electromagnetic coupling. The latter are known as partial inductances and potential coefficients [7]. Since the PEEC method is based on the principle of volume equivalence, the currents and charges are assumed to radiate in the background medium, and therefore, free-space Green's function has to be considered. If the quasi-static assumption can be done, for electrically small problems (e.g., involving low frequencies and/or geometrically small structures), Green's function simplifies and the partial elements become frequency independent. If an orthogonal mesh is used, analytical formulas are available for both partial inductances L_p and coefficients of potential P [7]. However, the existing analytical formulas are affected by significant numerical errors for certain PEEC structural mesh necessary to model the skin and proximity effects with higher accuracy. In [8], a systematic strategy to select a proper analytical formula depending on the dimensions and positions of two elementary volumes is proposed for the accurate computation of partial inductances under the quasi-static hypothesis.

When the quasi-static hypothesis is not valid longer, full-wave Green's function has to be considered. In this case, the calculation of the partial elements modeling the magnetic and electric field couplings, L_p and P, respectively, is normally carried out by using numerical integration, which, however, is very computationally expensive. This limitation can be overcome by using Taylor expansion, as presented in [9]. Nevertheless, similar numerical issues can also be found in the full-wave calculation of the partial elements based on Taylor expansion. The aim of this article is to define a multifunction strategy that allows preserving the accuracy in the calculation of the coefficients of Taylor expansion of the partial elements as the frequency, size, and distance between the domains vary. An orthogonal mesh is assumed in this article.

The rest of this article is organized as follows. Section II summarizes the problems in the computation of integrals involved in the mutual partial inductance between two elementary parallelepipeds and the conditions to be used to set a correct strategy preserving the accuracy of the quasi-static partial inductance. The details of the computation of the Taylor series expansion coefficients, for different domains, e.g., volumes, surfaces, and lines, are given in Section III along with the strategy proposed to switch from one to another analytical formula in the different

Manuscript received 6 December 2022; revised 21 April 2023; accepted 19 May 2023. Date of publication 12 June 2023; date of current version 15 August 2023. This work was supported by the Swiss National Science Foundation under Grant 209501. *(Corresponding author: Giulio Antonini.)*

Daniele Romano and Giulio Antonini are with the UAq EMC Laboratory, Department of Industrial and Information Engineering and Economics, University of L'Aquila, I-67100 L'Aquila, Italy (e-mail: daniele.romano.vis@gmail.com; giulio.antonini@univaq.it).

Ivana Kovacevic-Badstuebner and Ulrike Grossner are with the Advanced Power Semiconductor Laboratory, ETH Zürich, 8092 Zürich, Switzerland (e-mail: kovacevic@aps.ee.ethz.ch; ulrike.grossner@ethz.ch).

Color versions of one or more figures in this article are available at https://doi.org/10.1109/TEMC.2023.3279423.

Digital Object Identifier 10.1109/TEMC.2023.3279423

scenarios. The range of applicability is described in Section IV along with an example. Finally, Section V concludes this article.

II. Mutual Partial Inductance Computation

In the quasi-static PEEC method, the magnetic field coupling between two elementary volumes i and j carrying uniform currents is described by the partial inductance, which requires the computation of the following double-folded volume integral:

$$L_{p_{i,j}} = \frac{\mu_0}{4\pi S_i S_j} \int_{V_i} \int_{V_j} \frac{1}{R} dV_j dV_i \tag{1}$$

where $R = ||R_i - R_j||$ is the distance between two points inside the two cells, and S_i and S_j are the cross sections normal to the current directions of two volumes i and j, respectively. When the quasi-static hypothesis is not satisfied, the full-wave computation is required. In this case, the coefficients (1) must consider the retardation through the exponential term, as shown in the following equation:

$$L_{p_{i,j}} = \frac{\mu_0}{4\pi S_i S_j} \underbrace{\int_{V_i} \int_{V_j} \frac{1}{R} e^{-j\beta R} dV_j dV_i}_{\mathcal{I}_{v-v}^{(\mathrm{FW})}} \tag{2}$$

where $\beta = 2\pi f \sqrt{\mu_0 \epsilon_0}$.

In [9], it is shown how it is possible to compute the coefficients (2) by resorting to the Taylor series expansion of the exponential term. In particular, the most efficient expansions reported in [9] work as described in the following. The double-folded integral $\mathcal{I}_{v-v}^{(\mathrm{FW})}$ in (2) is rewritten into an equivalent form as follows:

$$\mathcal{I}_{v-v}^{(\mathrm{FW})} = \int_{V_i} \int_{V_j} \frac{1}{R} e^{-j\beta(R-Rcc)} e^{-j\beta R_{cc}} dV_j dV_i \tag{3}$$

where R_{cc} is the center-to-center distance between the two volumes. Then, the term $e^{-j\beta R_{cc}}$ is approximated with its Taylor expansion, and it is moved out the integral, leading to

$$\mathcal{I}_{v-v}^{(\mathrm{FW})} = e^{-j\beta R_{cc}} \int_{V_i} \int_{V_j} \frac{1}{R} \left[1 - j\beta\hat{R} - \frac{\beta^2 \hat{R}^2}{2} + j\frac{\beta^3 \hat{R}^3}{6} \right] dV_j dV_i \tag{4}$$

where $\hat{R} = R - R_{cc}$.

By performing some trivial algebraic manipulations, it follows that

$$\begin{aligned} \mathcal{I}_{v-v}^{(\mathrm{FW})} = e^{-j\beta R_{cc}} \Bigg\{ & \mathcal{I}_{v-v}^{(QS)} + j\beta \left[\mathcal{I}_{v-v}^{(QS)} R_{cc} - \mathcal{I}_{v-v}^{(o1)} \right] \\ & + \beta^2 \left[-\frac{1}{2} \mathcal{I}_{v-v}^{(QS)} R_{cc}^2 + \mathcal{I}_{v-v}^{(o1)} R_{cc} - \frac{1}{2} \mathcal{I}_{v-v}^{(o2)} \right] + \frac{1}{2} j\beta^3 \cdot \\ & \cdot \left[-\frac{1}{3} \mathcal{I}_{v-v}^{(QS)} R_{cc}^3 + \mathcal{I}_{v-v}^{(o1)} R_{cc}^2 - L_{p_{ij}}^{(o2)} R_{cc} + \frac{1}{3} \mathcal{I}_{v-v}^{(o3)} \right] \Bigg\} \end{aligned} \tag{5}$$

where

$$\mathcal{I}_{v-v}^{(QS)} = \int_{V_i} \int_{V_j} \frac{1}{R} dV_j dV_i \tag{6a}$$

$$\mathcal{I}_{v-v}^{(o1)} = \int_{V_i} \int_{V_j} 1 dV_j dV_i = V_j V_i \tag{6b}$$

$$\mathcal{I}_{v-v}^{(o2)} = \int_{V_i} \int_{V_j} R dV_j dV_i \tag{6c}$$

$$\mathcal{I}_{v-v}^{(o3)} = \int_{V_i} \int_{V_j} R^2 dV_j dV_i. \tag{6d}$$

Integrals in (6) are frequency independent, and hence, they are computed only once and then used to compute a full-wave coefficient at any frequency. The analytical formulas for integrals (6), in the case of orthogonal volumes, are provided in [9] and [10]. The case of nonorthogonal volumes can be handled in two ways, in addition to the brute-force numerical integration.

1) The coefficients of Taylor expansion are computed once at the beginning and reused at different frequencies.
2) As a second option, a fine orthogonal mesh is used to approximate the nonorthogonal objects. Thus, the number of elementary unknowns can be very high. Such an approach is usually used in conjunction with an iterative method, in which the matrix–vector products are accelerated, e.g., via fast Fourier transform (FFT) [11], [12], [13], [14].

A. Problems in the Analytical Evaluation of Integrals (6)

Let us consider the following example, also presented in [8] for the quasi-static case. In particular, it considers two volumetric cells arranged as follows.

1) The dimensions of the first cell are $s_{x1} = 10$ μm, $s_{y1} = 4$ mm, $s_{z1} = 0.8$ μm.
2) The dimensions of the second cell are $s_{x2} = 1$ μm, $s_{y2} = 10$ μm, and $s_{z2} = sx_2/k$, where k ranges from 10^{-6} to 1, i.e., sz_2 varies in the range from 1 μm to 1 m.
3) The distance between the cells in x, y, and z directions is $\Delta x = s_{x1} \cdot h$, where h ranges from 10^{-2} to 10^5, $\Delta y = 0$, and $\Delta z = 0$, i.e., the minimum distance between cells $R_{\min}$ varies between 0.1 μm and 1 m.

For all these geometrical configurations, the computation of integrals in (6) is performed in the standard double-precision arithmetic by using the analytical solution provided in [9] and [10], while the reference values are computed using the Symbolic MATLAB Toolbox [15] (with at least 32 digits). The result of such test is reported in Fig. 1 .

In particular, for orthogonal volumes, when integrals (6) are computed in double precision, some numerical errors occur [16], [17]. More recently, Kovacevic-Badstuebner et al. [8] have proposed a technique that solves definitively the numerical problems related to the analytical computation of $\mathcal{I}_{v-v}^{(QS)}$.

The behavior of this approach has been summarized in Appendix A for completeness.

III. Improved Integral (6) Evaluation

The novelty of this article is to extend the technique presented in [8] for the computation of integrals $\mathcal{I}_{v-v}^{(o2)}$ and $\mathcal{I}_{v-v}^{(o3)}$ (6). To this aim, the closed-form solutions for these integrals when suppressing one or more dimensions at the time are needed. Similarly to the definitions made in (13), for $\mathcal{I}_{v-v}^{(o2)}$ and $\mathcal{I}_{v-v}^{(o3)}$, we will have: surface–volume $\mathcal{I}_{s-v}^{(o2)}$ and $\mathcal{I}_{s-v}^{(o3)}$, surface–surface $\mathcal{I}_{s-s}^{(o2)}$ and $\mathcal{I}_{s-s}^{(o3)}$, line–volume $\mathcal{I}_{\ell-v}^{(o2)}$ and $\mathcal{I}_{\ell-v}^{(o3)}$, point–volume

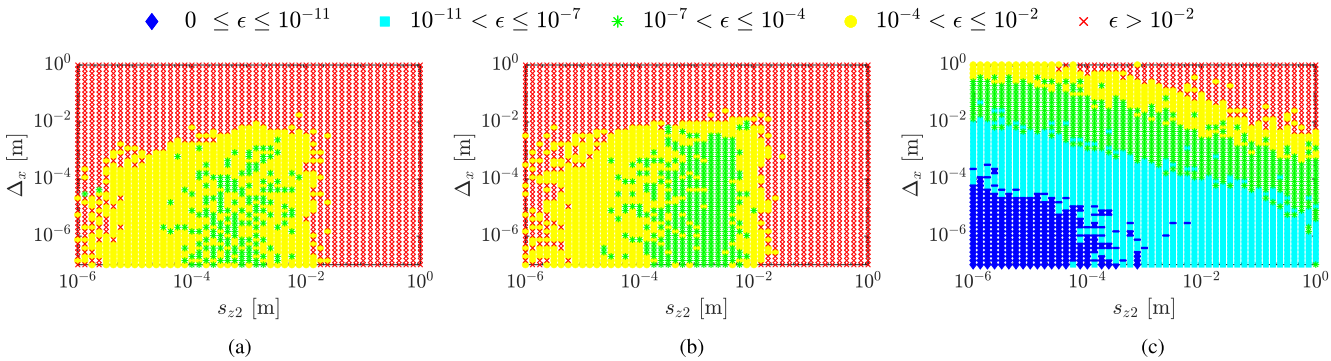

Fig. 1. Closed-form solution evaluation error for the integrals defined in (6) when the double-precision arithmetic is used for their computation. (a) $\mathcal{I}_{v-v}^{(QS)}$. (b) $\mathcal{I}_{v-v}^{(o2)}$. (c) $\mathcal{I}_{v-v}^{(o3)}$.

$\mathcal{I}_{p-v}^{(o2)}$ and $\mathcal{I}_{p-v}^{(o3)}$, line–surface $\mathcal{I}_{\ell-s}^{(o2)}$ and $\mathcal{I}_{\ell-s}^{(o3)}$, point–surface $\mathcal{I}_{p-s}^{(o2)}$ and $\mathcal{I}_{p-s}^{(o3)}$, line–line $\mathcal{I}_{\ell-\ell}^{(o2)}$ and $\mathcal{I}_{\ell-\ell}^{(o3)}$, point–line $\mathcal{I}_{p-\ell}^{(o2)}$ and $\mathcal{I}_{p-\ell}^{(o3)}$, and point–point $\mathcal{I}_{p-p}^{(o2)}$ and $\mathcal{I}_{p-p}^{(o3)}$, respectively.

The closed-form solutions for all these integrals, that represent the major novelty introduced in this article, are provided in Appendix B for the sake of readability.

A. *Improved $\mathcal{I}_{v-V}^{(o2)}$ and $\mathcal{I}_{v-V}^{(o3)}$ Evaluation*

The strategy introduced in [8] (summarized in Appendix A for $\mathcal{I}_{v-v}^{(QS)}$) can be applied to the integrals $\mathcal{I}_{v-v}^{(o2)}$ and $\mathcal{I}_{v-v}^{(o3)}$, defined in (6), by exploiting the formulas defined in Figs. 12–15. The main difference with $\mathcal{I}_{v-v}^{(QS)}$ described in [8] relies on the choice of the thresholds ϵ_1, ϵ_2, ϵ_3, and ϵ_4 required by the algorithm for the suppression reported in Fig. 11, while condition$_1$ (14a) for $\mathcal{I}_{v-v}^{(o2)}$ and $\mathcal{I}_{v-v}^{(o3)}$ is calculated following the same derivation procedure as applied to $\mathcal{I}_{v-v}^{(QS)}$. In particular, we have the following.

1) The correct evaluation of $\mathcal{I}_{v-v}^{(QS)}$ is obtained with the thresholds $\epsilon_1 = 10^{-3}$, $\epsilon_2 = 5 \times 10^{-3}$, $\epsilon_3 = 10^{-3}$, and $\epsilon_4 = 3 \times 10^{-1}$.
2) The same thresholds used for $\mathcal{I}_{v-v}^{(QS)}$ are used also for the integral $\mathcal{I}_{v-v}^{(o2)}$. This is due to the fact that each analytical solution of the integrals for $\mathcal{I}_{v-v}^{(QS)}$, that can be found in [8] and [17], defined in (13), has a similar counterpart in the solution of the integrals for $\mathcal{I}_{v-v}^{(o2)}$, given in [9] and Figs. 12–15, in the sense that there are similar summations of terms having the same exponential values. This is also confirmed by the similar error map that can be observed in Fig. 1(a) and (b). Moreover, condition$_1$ (14a) in this case is the following:

$$\text{condition}_1 = V_1 V_2 \frac{d_{n12,\max}}{R_{\min}} < \epsilon_1. \tag{7}$$

3) Finally, for integral $\mathcal{I}_{v-v}^{(o3)}$, from Fig. 1(c), it can be observed that more relaxed thresholds of suppression can be used since its computation fails for higher values of sizes and distances. Experimentally, by running a very large set of test cases, the best thresholds found for the suppression strategy are the following: $\epsilon_1 = 10^{-4}$, $\epsilon_2 = 3 \times 10^{-4}$, $\epsilon_3 = 10^{-3}$, and $\epsilon_4 = 3 \times 10^{-1}$. Furthermore, condition$_1$ (14a) in this case reads

$$\text{condition}_1 = 2V_1 V_2 d_{n12,\max} < \epsilon_1. \tag{8}$$

Hence, by applying the proposed technique to the same example of Section II-A, with the reported choice of thresholds, we obtain the results summarized in Fig. 2, where, also in this case, the reference values are computed using the Symbolic MATLAB Toolbox [15] (with at least 32 digits).

As seen, applying the proposed strategy for the computation of integrals (6) leads to very low errors. This allows us to conclude that the evaluation of (5) is affected now only by the Taylor expansion truncation of the exponential term and not by the digits of precision used in the evaluation of integrals (6).

IV. Numerical Tests

A. *Evaluation of the Range of Applicability*

The range of applicability of the proposed formulas when using the double- or quadruple-precision arithmetic is analyzed by calculating the integral (5) for different volumes sizes and distances. In particular, the distance between two cubic volumes is varied in the range from 0 to 1 m leading to 30 geometrical configurations. Such distance is calculated between the two nearest edges of the two volumes. In addition, the tests are performed for the edge size of the two volumes ranging from 10 μm to 1 mm. In the presented analysis, the integrals are computed based on five different approaches.

1) *Numerical:* The integral $\mathcal{I}_{v-v}^{(\text{FW})}$ in (2) is calculated through the adaptive numerical integration of MATLAB with an error threshold set to 10^{-9}. In particular, the integration is performed with the Gauss–Kronrod quadrature formula [18], where the adaptive strategy is implemented with seven evaluation Gauss points and 15 evaluation Kronrod points.

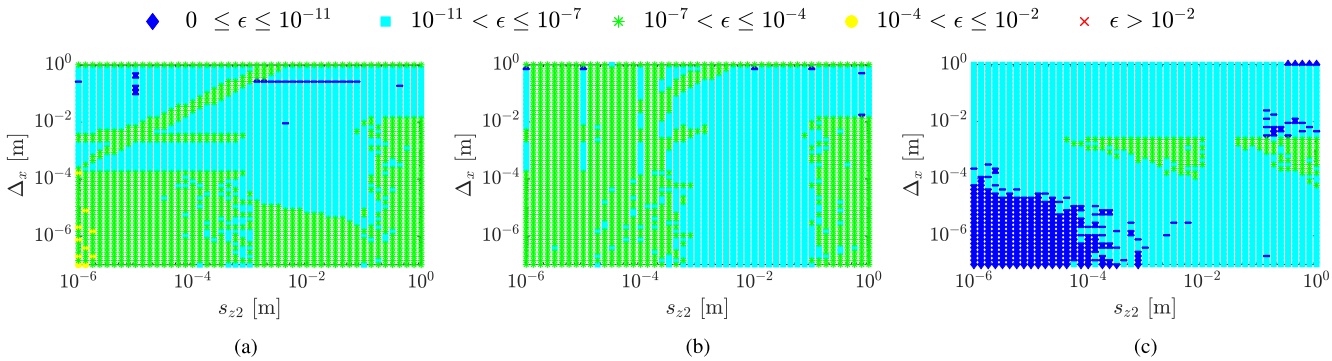

Fig. 2. Closed-form solution evaluation error for the integrals defined in (6) when the double-precision arithmetic is used for their computation together with the proposed strategy. (a) $\mathcal{I}_{v-v}^{(QS)}$. (b) $\mathcal{I}_{v-v}^{(o2)}$. (c) $\mathcal{I}_{v-v}^{(o3)}$.

2) *Double Taylor:* The integral $\mathcal{I}_{v-v}^{(\mathrm{FW})}$ in computed as reported in (5) by computing the integrals (6) by using the double-precision arithmetic.
3) *Quad Taylor:* The integral $\mathcal{I}_{v-v}^{(\mathrm{FW})}$ in computed as reported in (5) by computing the integrals (6) by using the quadruple-precision arithmetic (at least 32 digits).
4) *Suppression Taylor:* The integral $\mathcal{I}_{v-v}^{(\mathrm{FW})}$ in computed as reported in (5) by computing the integrals (6) by using the double-precision arithmetic together with the proposed suppression strategy, as reported in Section III.
5) *Proposed Taylor:* It works like Suppression Taylor with the difference that the integral $\mathcal{I}_{v-v}^{(\mathrm{FW})}$ is approximated as

$$\mathcal{I}_{v-v}^{(\mathrm{FW})} \simeq \mathcal{I}_{v-v}^{(QS)} e^{-j\beta R_{cc}} \tag{9}$$

when the following condition is satisfied:

$$R_{cc} > 50 s_{\max} \text{ and } f > \frac{1}{10} \cdot \frac{c_0}{30 s_{\max}}. \tag{10}$$

In (10), c_0 denotes the speed of light in free space, f denotes the frequency, and $s_{\max}$ denotes the largest value between the lengths, the widths, and the thickness of the two bars, for which $\mathcal{I}_{v-v}^{(\mathrm{FW})}$ is computed. Clearly, the integral $\mathcal{I}_{v-v}^{(QS)}$ in (9) is computed by adopting the suppression strategy given in [8]. Finally, the validity of the approximation (9), along with the condition (10), has been proven by running a large number of numerical tests.

The CPU times required for these methods are summarized in Table I along with the details of the frequency range and frequency samples for each case. Their computation has been carried out in MATLAB on a PC equipped with two physical processors operating at 3.46 GHz. From Table I, it is evident that the use of Taylor expansion with the double-precision arithmetic is extremely advantageous in terms of performances, while an accurate numerical integration is prohibitive.The accuracy of the Double Taylor, Quad Taylor, Suppression Taylor, and Proposed Taylor approaches is defined by a relative error computed as

$$\epsilon = \frac{|h_{\mathrm{TAYLOR}}| - |h_{\mathrm{NUMERICAL}}|}{|h_{\mathrm{NUMERICAL}}|}. \tag{11}$$

TABLE I
CPU TIME REQUIRED FOR CALCULATING THE INTEGRALS BASED ON THE TAYLOR AND NUMERICAL APPROACHES FOR THE DESCRIBED TEST CASES OF 30 GEOMETRICAL CONFIGURATIONS

	edge length		
	10 μm	100 μm	1 mm
Frequency range	A	B	C
Frequency samples #	12	10	8
CPU time—NUMERICAL	17 h	16 h	18 h
CPU time—QUAD	5 m	4 m	3 m
CPU time—DOUBLE	$<$ 20 ms	$<$ 17 ms	$<$ 15 ms
CPU time—SUPPRESSION	$<$ 40 ms	$<$ 35 ms	$<$ 30 ms
CPU time—PROPOSED	$<$ 40 ms	$<$ 35 ms	$<$ 30 ms

Frequency range: A: 10 MHz to 1 THz, B: 10 MHz to 100 GHz, and C: 10 MHz to 15 GHz.

where the numerical reference solution $h_{\mathrm{NUMERICAL}}$ is computed with the MATLAB adaptive integration with a relative error threshold set to 10^{-9}. The relative errors for Double Taylor, Quad Taylor, Suppression Taylor, and Proposed Taylor methods are shown in Figs. 3– 5 for the described test cases. In this analysis, the maximum frequency $f_{\max}$ has been chosen according with the $\lambda/30$ criterion; in particular, we have

$$s_{\max} < \frac{c_0}{30 f_{\max}} \tag{12}$$

where the same notation of (10) has been used.

As can be clearly seen from Figs. 3(d), 4(d), and 5(d), the proposed strategy always guarantees an error below 0.1%. Furthermore, it is evident that the Quad Taylor approach can be used as a reference method if the $\lambda/30$ criterion (12) is satisfied.

The following examples demonstrate how the calculation of $\mathbf{L}_p$ and $\mathbf{P}$ matrices influences the calculated vectors of currents and potentials. These coefficients are computed in C++, and more specifically, they are computed in parallel on seven threads in order to accelerate all the simulations.

B. Example 1: Coplanar Stripline Example

As the first example, a coplanar stripline structure described in Fig. 6 is modeled. The conductive ground, the lines, and the plate above the structure are made of copper. In addition, the

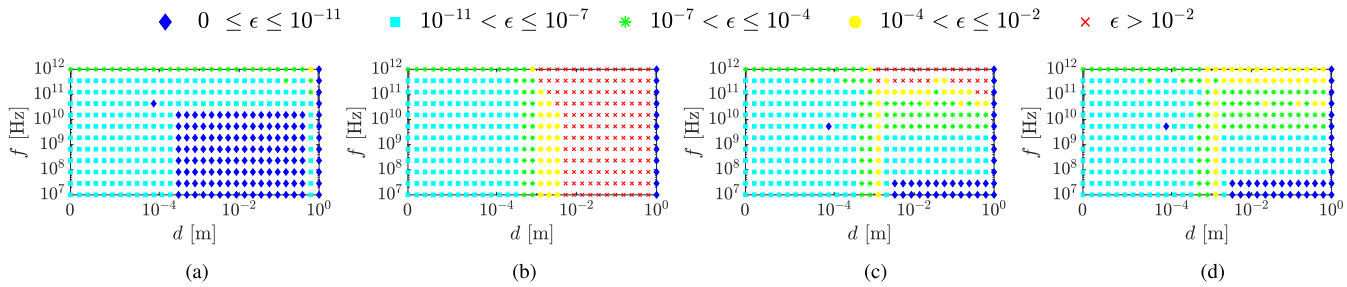

Fig. 3. Error evaluation for the cubic volume case with an edge of 10μm. (a) Quad Taylor. (b) Double Taylor. (c) Suppression Taylor. (d) Proposed Taylor.

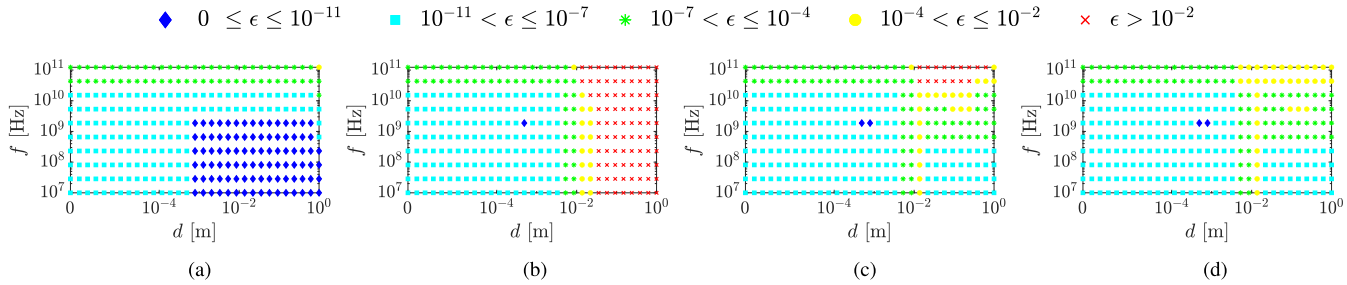

Fig. 4. Error evaluation for the cubic volumes case with an edge of 100μm. (a) Quad Taylor. (b) Double Taylor. (c) Suppression Taylor. (d) Proposed Taylor.

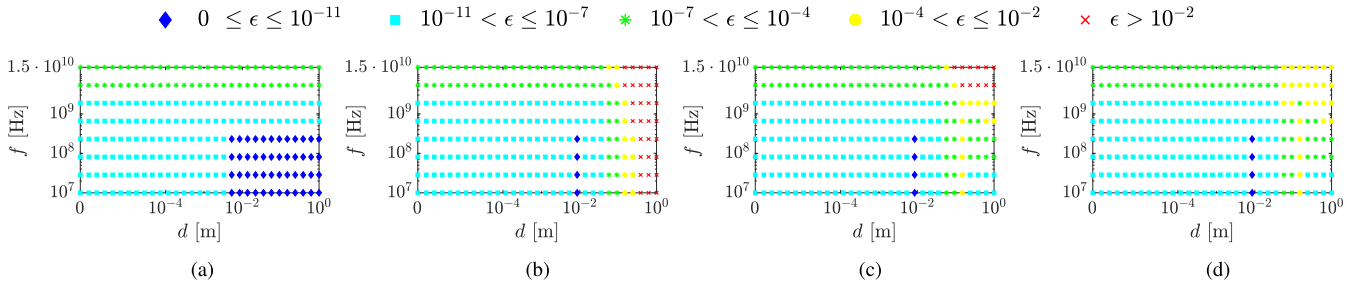

Fig. 5. Error evaluation for the cubic volumes case with an edge of 1 mm. (a) Quad Taylor. (b) Double Taylor. (c) Suppression Taylor. (d) Proposed Taylor.

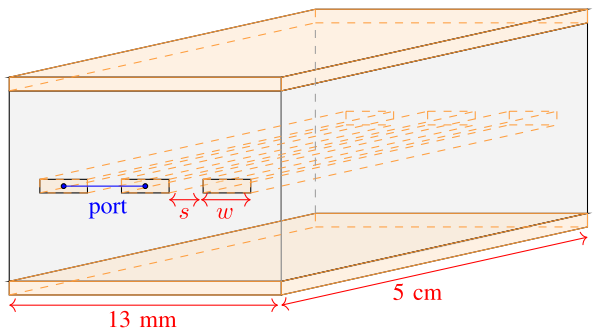

Fig. 6. Second modeling example: a coplanar stripline structure where the thickness of the dielectric is 2.7 mm and the thickness of all the conductors is 50μm. Finally, $s = 2$ mm and $w = 1$ mm.

lines are embedded into a dielectric with relative permittivity $\epsilon_r = 4$. All the geometrical details are given in Fig. 6.

The PEEC analysis has been performed from 100 MHz to 5 GHz by using a nonuniform mesh (with minimum mesh size of 0.4 μm and maximum mesh size of 1.5 mm in each direction) resulting in 25 680 PEEC inductive branches and 8688 capacitive surfaces.

The CPU time and relative error for the double-folded integrals used to fill $\mathbf{L}_p$ and $\mathbf{P}$ matrices (2)–(6) are summarized in Table II showing that the use of quadruple-precision computation leads to a high computation time, while the proposed solution shows a drastic reduction in the computation times. In addition, the Proposed Taylor approach is also faster than the Double Taylor, since, when several integration dimensions are suppressed, the derived closed formula evaluation requires less operations than the standard volume–volume integral solution.

The choice of the integrals used to fill $\mathbf{L}_p$ and $\mathbf{P}$ matrices by the Proposed Taylor method, between the developed closed formulas given in Appendix B, is summarized in Table III. In

TABLE II
CPU TIME AND RELATIVE ERROR FOR THE DOUBLE-FOLDED INTEGRALS USED TO FILL $\mathbf{L}_p$ AND $\mathbf{P}$ MATRICES (2)–(6) FOR THE COPLANAR STRIPLINE EXAMPLE

	CPU time			relative error	
	QUAD	DOUBLE	PROP	DOUBLE	PROP
$\mathcal{I}^{(\mathbf{QS})}_{\mathbf{s-s}}$	23 h	12 s	9 s	1.4×10^{-3}	3.9×10^{-8}
$\mathcal{I}^{(\mathbf{o2})}_{\mathbf{s-s}}$	23 h	12 s	10 s	1.1×10^{-4}	4.1×10^{-8}
$\mathcal{I}^{(\mathbf{o3})}_{\mathbf{s-s}}$	24 m	5 s	5 s	3.1×10^{-7}	2.8×10^{-10}
$\mathcal{I}^{(\mathbf{QS})}_{\mathbf{v-v}}$	10 d	194 s	88 s	6.9	1.2×10^{-7}
$\mathcal{I}^{(\mathbf{o2})}_{\mathbf{v-v}}$	10 d	196 s	96 s	0.8	1.2×10^{-7}
$\mathcal{I}^{(\mathbf{o3})}_{\mathbf{v-v}}$	102 m	17 s	19 s	5.3×10^{-5}	5.7×10^{-9}

Abbreviations: m: minutes, h: hours, d: days, QUAD: Quad Taylor, DOUBLE: Double Taylor, PROP: Proposed Taylor.

TABLE III
SELECTED CLOSED FORMULAS, IN PERCENTAGE, TO FILL $\mathbf{L}_p$ AND $\mathbf{P}$ MATRICES (6), WITH THE PROPOSED TAYLOR METHOD, FOR THE COPLANAR STRIPLINES EXAMPLE

	$\mathbf{L}_p$		$\mathbf{P}$	
	$\mathcal{I}^{(QS)}_{v-v}$ / $\mathcal{I}^{(o2)}_{v-v}$ %	$\mathcal{I}^{(o3)}_{v-v}$ %	$\mathcal{I}^{(QS)}_{s-s}$ / $\mathcal{I}^{(o2)}_{s-s}$ %	$\mathcal{I}^{(o3)}_{s-s}$ %
$\mathcal{I}_{\mathbf{p-p}}$	0	0	< 1	< 1
$\mathcal{I}_{\mathbf{p}-\ell}$	< 1	0	1.3	< 1
$\mathcal{I}_{\mathbf{p-s}}$	< 1	0	2.5	< 1
$\mathcal{I}_{\mathbf{p-v}}$	< 1	0	–	–
$\mathcal{I}_{\ell-\ell}$	< 1	< 1	9.3	< 1
$\mathcal{I}_{\ell-\mathbf{s}}$	5.8	< 1	40.9	12.6
$\mathcal{I}_{\ell-\mathbf{v}}$	3	< 1	–	–
$\mathcal{I}_{\mathbf{s-s}}$	36.2	< 1	45.8	85.9
$\mathcal{I}_{\mathbf{s-v}}$	38.5	12	–	–
$\mathcal{I}_{\mathbf{v-v}}$	16.3	86.4	–	–

this example, the approximation (9) is practically unused since less than 1% of coefficients are corrected with it, and hence, the accuracy is reached by only applying the suppression strategy introduced in Section III.

In the next step, the accuracy in the computation of currents and voltages between a node of the structures and all the other nodes is evaluated for the Double Taylor and Proposed Taylor approaches. The errors are computed by using (11) and presented in Fig. 7. In this case, Fig. 7 demonstrates how the errors in $\mathbf{L}_p$ matrix influence the calculation of the current distribution, while the error on voltage distribution is less influent for the same reasoning given in [8].

In any case, the errors of the current distributions have a significant impact on the postprocessing step to calculate electromagnetic fields.

C. Example 2: Microstrip Line Example

As the second example, a microstrip line structure described in Fig. 8 is modeled. The conductors are made of copper (conductivity $\sigma = 5.8 \times 10^7$), while the dielectric substrate is made of the standard FR4 material ($\epsilon_r = 4.2$ and $\tan\delta = 0.02$).

The PEEC analysis has been performed from 500 MHz to 5 GHz by using an orthogonal mesh approach, in which all the structures are discretized into voxels (that are practically rectangular bars) having all the same sizes. The sizes of the voxels along the x, y, and z axes are $s_x = 84\mu$m, $s_y = 384\mu$m,

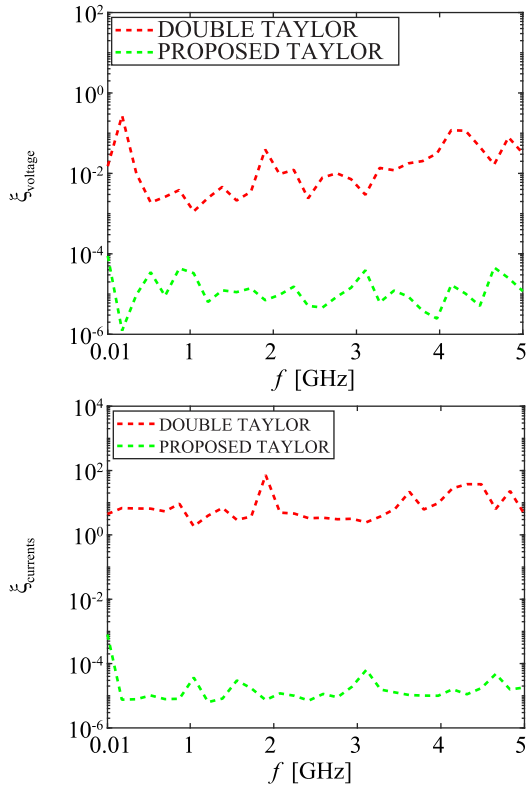

Fig. 7. ϵ-errors of the current and voltage vectors for the coplanar stripline example.

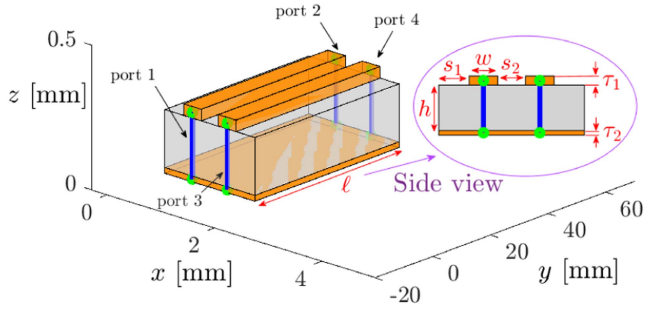

Fig. 8. Geometry of the microstrip line example. Geometrical parameters: $s_1 = 0.35, s_2 = 0.32, w = 0.33, \ell = 50, h = 0.2, \tau_1 = 0.04$, and $\tau_2 = 0.02$ (all the dimensions are in millimeters).

and $s_z = 10\mu$m, respectively. In particular, the mesh is achieved through a rectangular grid having $N_x = 20$, $N_y = 140$, and $N_z = 26$, where N_x, N_y, and N_z are the number of voxels along the x, y, and z axes, respectively, resulting in 186 288 inductive branches, 18 864 capacitive surfaces, and 61 600 nodes. Since the mesh is made by a regular 3-D grid in which all the voxels have the same size, we can use an iterative solver in which the matrix–vector products can be accelerated through the FFT [11], [12], [13], [14]. In particular, we use the generalized minimal residual method (GMRES) iterative solver, as described in detail in [11], with the threshold of convergence set to 10^{-4} and with the maximum number of iterations set to 3000. Since the matrix–vector products are performed via FFT, it follows that

TABLE IV
CPU TIME AND RELATIVE ERROR FOR THE DOUBLE-FOLDED INTEGRALS USED TO FILL THE ROWS OF $\mathbf{L}_p$ AND $\mathbf{P}$ MATRICES (2)–(6) FOR THE MICROSTRIP LINE EXAMPLE

	CPU time			relative error	
	QUAD	DOUBLE	PROP	DOUBLE	PROP
$\mathcal{I}^{(\mathbf{QS})}_{\mathbf{s-s}}$	12 m	<1 ms	<1 ms	0.01	3×10^{-7}
$\mathcal{I}^{(\mathbf{o2})}_{\mathbf{s-s}}$	12 m	<1 ms	<1 ms	0.04	6.5×10^{-7}
$\mathcal{I}^{(\mathbf{o3})}_{\mathbf{s-s}}$	33 s	<1 ms	<1 ms	1.9×10^{-7}	1.9×10^{-7}
$\mathcal{I}^{(\mathbf{QS})}_{\mathbf{v-v}}$	10 m	<1 ms	<1 ms	0.1	2.9×10^{-7}
$\mathcal{I}^{(\mathbf{o2})}_{\mathbf{v-v}}$	10 m	<1 ms	<1 ms	0.3	7×10^{-7}
$\mathcal{I}^{(\mathbf{o3})}_{\mathbf{v-v}}$	26 s	<1 ms	<1 ms	1.8×10^{-7}	1.8×10^{-7}

Abbreviations: m: minutes, h: hours, QUAD: Quad Taylor, DOUBLE: Double Taylor, and PROP: Proposed Taylor.

TABLE V
SELECTED CLOSED FORMULAS, IN PERCENTAGE, TO FILL $\mathbf{L}_p$ AND $\mathbf{P}$ MATRICES (6), WITH THE PROPOSED TAYLOR METHOD, FOR THE MICROSTRIP LINE EXAMPLE

	$\mathbf{P}$		$\mathbf{L}_p$	
	$\mathcal{I}^{(QS)}_{s-s}$ / $\mathcal{I}^{(o2)}_{s-s}$ %	$\mathcal{I}^{(o3)}_{s-s}$ %	$\mathcal{I}^{(QS)}_{v-v}$ / $\mathcal{I}^{(o2)}_{v-v}$ %	$\mathcal{I}^{(o3)}_{v-v}$ %
$\mathcal{I}_{\mathbf{p-p}}$	4.3	0	0	0
$\mathcal{I}_{\mathbf{p}-\ell}$	35.1	0	0	0
$\mathcal{I}_{\mathbf{p-s}}$	0	0	0	0
$\mathcal{I}_{\mathbf{p-v}}$	–	–	–	–
$\mathcal{I}_{\ell-\ell}$	38.4	13.1	65.3	0
$\mathcal{I}_{\ell-\mathbf{s}}$	16	17.4	0	0
$\mathcal{I}_{\ell-\mathbf{v}}$	–	–	0	0
$\mathcal{I}_{\mathbf{s-s}}$	6.2	69.5	30	32
$\mathcal{I}_{\mathbf{s-v}}$	–	–	0	0
$\mathcal{I}_{\mathbf{v-v}}$	–	–	4.7	68

just one matrix row needs to be computed and stored to build the circulant tensors required for the matrix–vector products involving the matrices $\mathbf{L}_p$ and $\mathbf{P}$ [12].

The CPU time and relative error for the double-folded integrals used to fill the rows of $\mathbf{L}_p$ and $\mathbf{P}$ matrices (2)–(6) are summarized in Table IV showing that the use of the quadruple-precision computation leads to a high computation time, while the double-precision computations are extremely fast (since, in this example, just few matrix rows are computed to build the circulant tensors).

The choice of the integrals used to fill $\mathbf{L}_p$ and $\mathbf{P}$ matrices by the Proposed Taylor method is summarized in Table V, where the notation is the same as used for Table III. Also, in this example, the approximation (9) is practically unused since less than 1% of coefficients are fixed by (9).

In addition, the scattering parameters are shown in Fig. 9. As can be clearly seen, the proposed solution shows a very good agreement with the Quad Taylor method, while the Double Taylor method leads to less accurate results at high frequency.

Finally, the number of GMRES iterations is shown in Fig. 10, in which it can be noted that the Quad Taylor method and the proposed method perform the same number of iterations, while the Double Taylor method exhibits a higher number of iterations reaching also the limit of 3000 iterations at high frequency without satisfying the 10^{-4} threshold used for the convergence criterion.

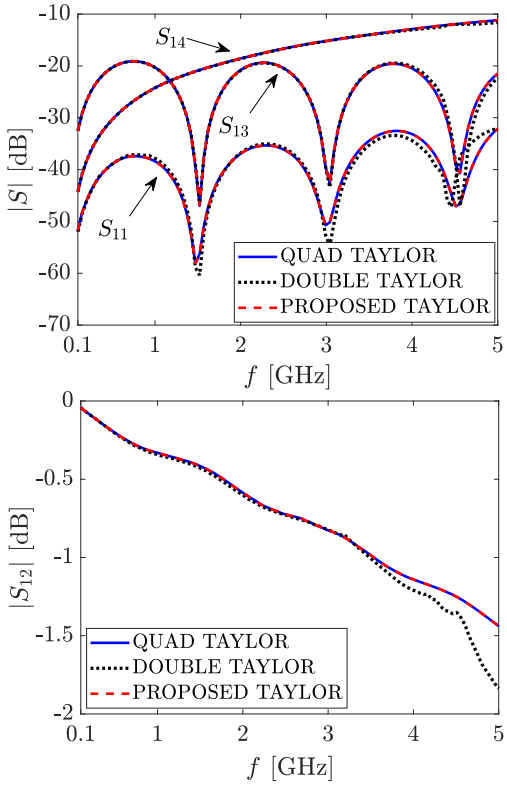

Fig. 9. Scattering parameters for the microstrip line example.

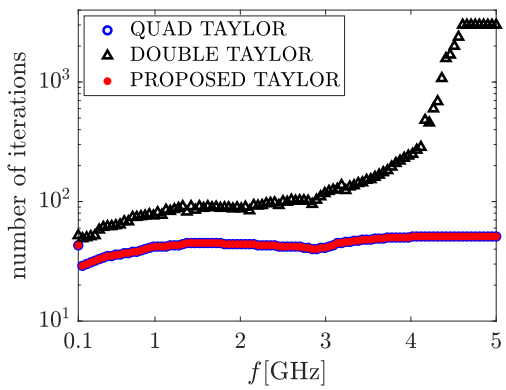

Fig. 10. Number of GMRES iterations for the microstrip line example.

Clearly, from this results, it is evident that an inaccurate subset of $\mathbf{L}_p$ and $\mathbf{P}$ coefficients has a negative impact on the convergence of an iterative method, which worsens with increasing frequency. This is a strong limitation because the use of an iterative method is strictly needed to solve problems with a large number of unknowns that appear for practical examples of 3-D circuit layouts.

V. CONCLUSION

In this article, the accuracy of PEEC electromagnetic models at high frequency has been significantly improved by exploiting and extending strategy for selecting the right analytical formula depending on the dimensions and positions of the two PEEC

elementary volumes/surfaces. This allows the computation of the interaction integrals with a relative error of less than 1%, avoiding the numerical integration and the quadruple-precision arithmetic. A provided set of analytical formulas, required by the technique, can also be useful to any other numerical method requiring double-folded volume or surface integrations of free-space Green's function over rectangular domains. Finally, the numerical results show that significant speedup is achieved while preserving the accuracy of the solution. In addition, the last example also highlights that inaccurate mutual coefficient computation can compromise the convergence of an iterative solver required to solve large computational problems.

Appendix A

Improved $\mathcal{I}_{v-V}^{(QS)}$ Evaluation

In [8], starting from the six-variable-folded integral $\mathcal{I}_{v-v}^{(QS)}$, a set of $I_{v-v}^{(qs)}$ formulas was developed by suppressing one or more dimensions at the time, which leads to nine special cases (13): surface–volume $\mathcal{I}_{s-v}^{(QS)}$, surface–surface $\mathcal{I}_{s-s}^{(QS)}$, line–volume $\mathcal{I}_{\ell-v}^{(QS)}$, point–volume $\mathcal{I}_{p-v}^{(QS)}$, line–surface $\mathcal{I}_{\ell-s}^{(QS)}$, point–surface $\mathcal{I}_{p-s}^{(QS)}$, line–line $\mathcal{I}_{\ell-\ell}^{(QS)}$, point–line $\mathcal{I}_{p-\ell}^{(QS)}$, and point–point $\mathcal{I}_{p-p}^{(QS)}$, where v, s, ℓ, and p stand for volume, surface, line, and point, respectively

$$\mathcal{I}_{v-v}^{(QS)} \approx \begin{cases} \ell_j \cdot \mathcal{I}_{s-v}^{(QS)} \\ \ell_j \ell_i \cdot \mathcal{I}_{s-s}^{(QS)} \\ \ell_{jk} \ell_{jm} \cdot \mathcal{I}_{\ell-v}^{(QS)} \\ \ell_{jk} \ell_{jm} \ell_{jn} \cdot \mathcal{I}_{p-v}^{(QS)} \\ \ell_{jk} \ell_{jm} \ell_i \cdot \mathcal{I}_{\ell-s}^{(QS)} \\ \ell_{jk} \ell_{jm} \ell_{jn} \ell_i \cdot \mathcal{I}_{p-s}^{(QS)} \\ \ell_{jk} \ell_{jm} \ell_{ik} \ell_{im} \cdot \mathcal{I}_{\ell-\ell}^{(QS)} \\ \ell_{jk} \ell_{jm} \ell_{jn} \ell_{ik} \ell_{im} \cdot \mathcal{I}_{p-\ell}^{(QS)} \\ \ell_{jk} \ell_{jm} \ell_{jn} \ell_{ik} \ell_{im} \ell_{in} \cdot \mathcal{I}_{p-p}^{(QS)} \end{cases} . \tag{13}$$

The algorithm needed to switch between the various formulas in (13) is given in [8] and reported in the following for completeness. By defining the following ϵ-condition:

$$\text{condition}_1 = V_1 V_2 \frac{d_{n12,\max}}{R_{\min}^3} < \epsilon_1 \tag{14a}$$

$$\text{condition}_2(s_{ni}) = s_{ni}/R_{\min} < \epsilon_2 \tag{14b}$$

$$\text{condition}_3(s_{ni}) = s_{ni}/\max(s_{xi}, s_{yi}, s_{zi}) < \epsilon_3 \tag{14c}$$

$$\text{condition}_\text{A} = \text{condition}_1 \textbf{ and } (\text{condition}_2 \textbf{ or } \text{condition}_3) \tag{14d}$$

the algorithm reported in Fig. 11 can be applied to understand what dimension must be suppressed for a volume.

Procedure: Reduce-Volume-Integral-Order

```
Input: s_xi, s_yi, s_zi, d_n12,max, V_1, V_2, R_min, ε_1-4
  a = min(s_xi,s_yi,s_zi)
  b = max(s_xi,s_yi,s_zi)
  c = mean(s_xi,s_yi,s_zi)
  if conditionA(a)
    Suppress a                  //n=2: Vol → Surf
    if (b/R_min < ε_4)
      if conditionA(c)
        Suppress c              //n=1: Surf → Lin
      end
      if conditionA(b)
        Suppress b              //n=0: Lin → Pnt
      end
    end
  end
```

Fig. 11. Reducing the volume (three-fold) integral for the volume cell i to either zero-fold, one-fold or two-fold integral depending on the cell dimensions and the distance to the other cell.

Appendix B

Closed Formulas for Integrals $\mathcal{I}_{v-V}^{(o2)}$ and $\mathcal{I}_{v-V}^{(o3)}$

The analytical solutions is the integrals $\mathcal{I}_{v-v}^{(o2)}$ and $\mathcal{I}_{v-v}^{(o3)}$ (6) are summarized in Figs. 12–15. It is important to underline that only the closed-form solutions are given, while all the algebraic steps performed to achieve them are skipped due to the lack of space.

Appendix C

Tips for Integral Evaluation

The evaluation of the integrals given in Figs. 12–15 must be performed as follows. The singularity of type $x \log\left(\sqrt{x^2+y^2+z^2}\right)$ is solved using

$$\lim_{x \to 0} \left[x \log\left(\sqrt{x^2+y^2+z^2}\right) \right] = 0. \tag{15}$$

Function $x^2 \tan^{-1}\left(\frac{yz}{x\sqrt{x^2+y^2+z^2}}\right)$ is evaluated as $x|x|\text{arctan2}\left(\frac{yz}{|x|\sqrt{x^2+y^2+z^2}}\right)$, where the function arctan2 is defined by

$$\text{arctan2}\left(\frac{k}{m}\right) = \begin{cases} \tan^{-1}\left(\frac{k}{m}\right), & \text{if } m > 0 \\ \tan^{-1}\left(\frac{k}{m}\right) + \pi, & \text{if } k \geq 0 \text{ and } m < 0 \\ \tan^{-1}\left(\frac{k}{m}\right) - \pi, & \text{if } k < 0 \text{ and } m < 0 \\ \frac{\pi}{2}, & \text{if } k > 0 \text{ and } m = 0 \\ -\frac{\pi}{2}, & \text{if } k < 0 \text{ and } m = 0 \end{cases} \tag{16}$$

with $\tan^{-1}(q)$ representing the inverse tangent of q computed in the range $[-\pi/2, \pi/2]$

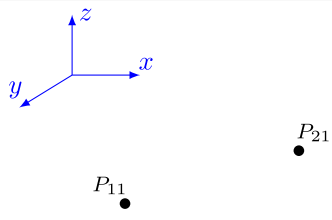

$P_{11} = (x_1, y_1, z_1)$; $P_{21} = (x_3, y_3, z_3)$

$$\mathcal{I}_{p-p}^{(o_2)} = \sqrt{(x_1 - x_3)^2 + (y_1 - y_3)^2 + (z_1 - z_3)^2}$$

$$\mathcal{I}_{p-p}^{(o_3)} = (x_1 - x_3)^2 + (y_1 - y_3)^2 + (z_1 - z_3)^2$$

(a)

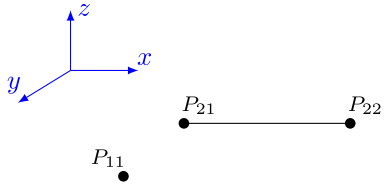

$P_{11} = (x_1, y_1, z_1)$
$P_{21} = (x_3, y_3, z_3)$; $P_{22} = (x_4, y_3, z_3)$

$$\mathcal{I}_{p-\ell}^{(o_2)} = \sum_{k=3}^{4} (-1)^{(k+1)} 1/2 \left[s_x R + (s_y^2 + s_z^2) \log(s_x + R) \right]$$

$$\mathcal{I}_{p-\ell}^{(o_3)} = \sum_{k=3}^{4} (-1)^{(k+1)} \left[1/3 s_x^3 + s_x (s_y^2 + s_z^2) \right]$$

where $s_x = x_1 - x_k$, $s_y = y_1 - y_3$, $s_z = z_1 - z_3$ and $R = \sqrt{s_x^2 + s_y^2 + s_z^2}$

(b)

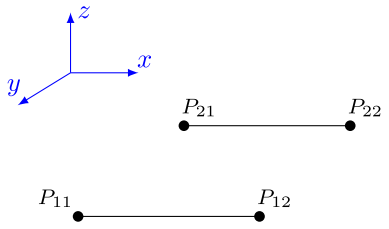

$P_{11} = (x_1, y_1, z_1)$; $P_{12} = (x_2, y_1, z_1)$
$P_{21} = (x_3, y_3, z_3)$; $P_{22} = (x_4, y_3, z_3)$

$$\mathcal{I}_{\ell-\ell}^{(o_2)} = \sum_{i=1}^{2} \sum_{k=3}^{4} \sum_{h=1}^{2} (-1)^{(i+k+1)} \gamma_h \quad ; \quad \gamma_1 = 1/3(1/2 s_x^2 - s_y^2 - s_z^2) R$$
$$\gamma_2 = 1/2 s_x (s_y^2 + s_z^2) \log(s_x + R)$$

$$\mathcal{I}_{\ell-\ell}^{(o_3)} = \sum_{i=1}^{2} \sum_{k=3}^{4} (-1)^{(i+k+1)} \left\{ 1/(12) s_x^2 \left[s_x^2 + 6(s_y^2 + s_z^2) \right] \right\}$$

where $s_x = x_i - x_k$, $y = y_1 - y_3$, $s_z = z_1 - z_3$ and $R = \sqrt{s_x^2 + s_y^2 + s_z^2}$

(c)

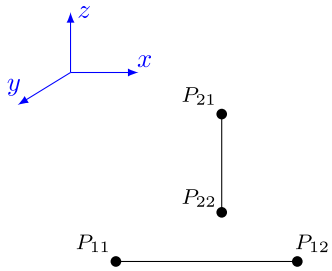

$P_{11} = (x_1, y_1, z_1)$; $P_{12} = (x_2, y_1, z_1)$
$P_{21} = (x_3, y_3, z_3)$; $P_{22} = (x_3, y_3, z_4)$

$$\mathcal{I}_{\ell-\ell}^{(o_2)} = \sum_{i=1}^{2} \sum_{n=3}^{4} \sum_{h=1}^{4} (-1)^{(i+n+1)} \gamma_h \quad ; \quad \gamma_1 = -1/3 s_z (s_y^2 - 1/6 s_z^2 - s_x R)$$
$$\gamma_2 = 1/6 s_z \left(3 s_y^2 + s_z^2\right) \log\left(s_x + R\right) \quad ; \quad \gamma_3 = 1/6 s_x \left(s_x^2 + 3 s_y^2\right) \log\left(s_z + R\right)$$
$$\gamma_4 = 1/3 s_y^3 \left[\arctan\left(\frac{s_z}{s_y}\right) - \arctan\left(\frac{s_x s_z}{s_y R}\right) \right]$$

$$\mathcal{I}_{\ell-\ell}^{(o_3)} = \sum_{i=1}^{2} \sum_{n=3}^{4} (-1)^{(i+n+1)} \left[1/3 s_x s_z (s_x^2 + 3 s_y^2 + s_z^2) \right]$$

where $s_x = x_i - x_3$, $s_y = y_1 - y_3$, $s_z = z_1 - z_n$ and $R = \sqrt{s_x^2 + s_y^2 + s_z^2}$

(d)

Fig. 12. Analytical formulas for point-point $\mathcal{I}_{p-p}^{(o_2)}$ and $\mathcal{I}_{p-p}^{(o_3)}$, line-point $\mathcal{I}_{p-\ell}^{(o_2)}$ and $\mathcal{I}_{p-\ell}^{(o_3)}$ and line-line $\mathcal{I}_{\ell-\ell}^{(o_2)}$ and $\mathcal{I}_{\ell-\ell}^{(o_3)}$ integrals, where $x_1 < x_2$, $x_3 < x_4$ and $z_3 < z_4$.(a) Analytical formulas for the point-point integrals. (b) Analytical formulas for the point-line integrals. (c) Analytical formulas for the parallel line-line integrals. (d) Analytical formulas for the orthogonal line-line integrals.

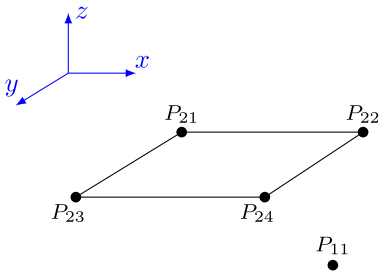

$P_{11} = (x_1, y_1, z_1)$
$P_{21} = (x_3, y_3, z_3)$; $P_{22} = (x_4, y_3, z_3)$
$P_{23} = (x_3, y_4, z_3)$; $P_{24} = (x_4, y_4, z_3)$

$$\mathcal{I}_{p-s}^{(o_2)} = \sum_{k=3}^{4}\sum_{m=3}^{4}\sum_{h=1}^{5}(-1)^{(k+m+1)}\gamma_h \quad ; \quad \gamma_1 = 1/3s_y(s_z^2 + 1/6s_y^2 - s_xR)$$
$$\gamma_2 = -1/6s_x\left(s_x^2 + 3s_z^2\right)\log\left(s_y + R\right) \quad ; \quad \gamma_3 = -1/6s_y\left(s_y^2 + 3s_z^2\right)\log\left(s_x + R\right)$$
$$\gamma_4 = -1/3s_z^3\arctan\left(\frac{s_y}{s_z}\right) \quad ; \quad \gamma_5 = 1/3s_z^3\arctan\left(\frac{s_xs_y}{s_zR}\right)$$

$$\mathcal{I}_{p-s}^{(o_3)} = \sum_{k=3}^{4}\sum_{m=3}^{4}(-1)^{(k+m)}\left[1/3s_xs_y(s_x^2 + s_y^2 + 3s_z^2)\right]$$

where $s_x = x_1 - x_k,\ s_y = y_1 - y_m,\ s_z = z_1 - z_2$ and $R = \sqrt{s_x^2 + s_y^2 + s_z^2}$

(a)

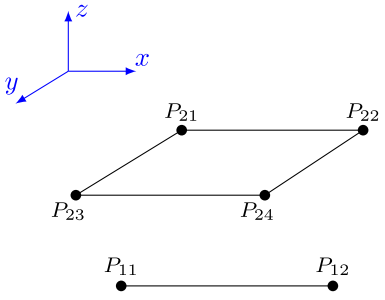

$P_{11} = (x_1, y_1, z_1)$; $P_{12} = (x_2, y_1, z_1)$
$P_{21} = (x_3, y_3, z_3)$; $P_{22} = (x_4, y_3, z_3)$
$P_{23} = (x_3, y_4, z_3)$; $P_{24} = (x_4, y_4, z_3)$

$$\mathcal{I}_{\ell-s}^{(o_2)} = \sum_{i=1}^{2}\sum_{k=3}^{4}\sum_{m=3}^{4}\sum_{h=1}^{5}(-1)^{(i+k+m+1)}\gamma_h$$
$$\gamma_1 = -1/3\left(1/6s_xs_y^3 + s_xs_ys_z^2\right) + 1/4\left(1/2s_x^2s_y - 1/3s_y^3 - 5/6s_ys_z^2\right)R$$
$$\gamma_2 = 1/2\left(1/3s_xs_y^3 + s_xs_ys_z^2\right)\log\left(s_x + R\right) \quad ; \quad \gamma_3 = 1/3s_xs_z^3\arctan\left(s_y/s_z\right)$$
$$\gamma_4 = 1/4\left(1/6s_x^4 + s_x^2s_z^2 - 1/2s_z^4\right)\log\left(s_y + R\right) \ ; \ \gamma_5 = -1/3s_xs_z^3\arctan\left(\frac{s_xs_y}{s_zR}\right)$$

$$\mathcal{I}_{\ell-s}^{(o_3)} = \sum_{i=1}^{2}\sum_{k=3}^{4}\sum_{m=3}^{4}(-1)^{(i+k+m+1)}\left[1/(12)s_x^2s_y(s_x^2 + 2s_y^2 + 6s_z^2)\right]$$

where $s_x = x_i - x_k,\ s_y = y_1 - y_m,\ s_z = z_1 - z_3$ and $R = \sqrt{s_x^2 + s_y^2 + s_z^2}$

(b)

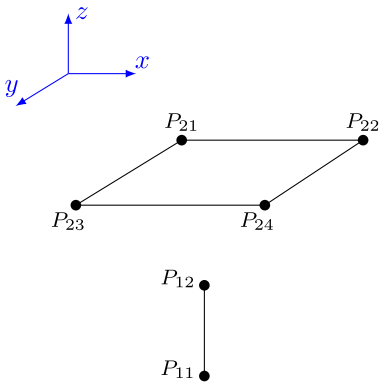

$P_{11} = (x_1, y_1, z_1)$; $P_{12} = (x_1, y_1, z_2)$
$P_{21} = (x_3, y_3, z_3)$; $P_{22} = (x_4, y_3, z_3)$
$P_{23} = (x_3, y_4, z_3)$; $P_{24} = (x_4, y_4, z_3)$

$$\mathcal{I}_{\ell-s}^{(o_2)} = \sum_{j=1}^{2}\sum_{k=3}^{4}\sum_{m=3}^{4}\sum_{h=1}^{8}(-1)^{(j+k+m)}\gamma_h$$
$$\gamma_1 = -1/(12)s_y^4\arctan\left(\frac{s_xs_z}{s_yR}\right)$$
$$\gamma_2 = -1/(12)s_x^4\arctan\left(\frac{s_ys_z}{s_xR}\right) \quad ; \quad \gamma_3 = -1/(12)s_z^4\arctan\left(\frac{s_xs_y}{s_zR}\right)$$
$$\gamma_4 = 1/6s_xs_y\left(s_x^2 + s_y^2\right)\log\left(s_z + R\right) \quad ; \quad \gamma_5 = 1/12\left(s_x^4 - s_y^4\right)\arctan\left(s_y/s_x\right)$$
$$\gamma_6 = 1/6s_ys_z\left(s_y^2 + s_z^2\right)\log\left(s_x + R\right) \quad ; \quad \gamma_7 = 1/6s_xs_z\left(s_x^2 + s_z^2\right)\log\left(s_y + R\right)$$
$$\gamma_8 = -1/(18)\left(5/2s_xs_y^3 + s_x^3s_z - 5/2s_x^3s_y\right) + 1/4s_xs_ys_zR$$

$$\mathcal{I}_{\ell-s}^{(o_3)} = \sum_{j=1}^{2}\sum_{k=3}^{4}\sum_{m=3}^{4}\sum_{h=1}^{8}(-1)^{(j+k+m)}\left[1/3s_xs_ys_z(s_x^2 + s_y^2 + s_z^2)\right]$$

where $s_x = x_1 - x_k,\ s_y = y_1 - y_m,\ s_z = z_j - z_3$ and $R = \sqrt{s_x^2 + s_y^2 + s_z^2}$

(c)

Fig. 13. Analytical formulas for point–surface $\mathcal{I}_{p-s}^{(o_2)}$ and $\mathcal{I}_{p-s}^{(o_3)}$ and line–surface $\mathcal{I}_{\ell-s}^{(o_2)}$ and $\mathcal{I}_{\ell-s}^{(o_3)}$ integrals, where $x_1 < x_2$, $z_1 < z_2$, $x_3 < x_4$, and $y_3 < y_4$. (a) Analytical formulas for the point–surface integrals. (b) Analytical formulas for the parallel line–surface integrals. (c) Analytical formulas for the orthogonal line–surface integrals.

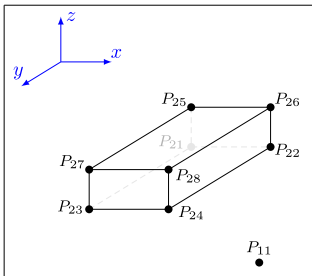

$P_{11} = (x_1, y_1, z_1)$
$P_{21} = (x_3, y_3, z_3)$; $P_{22} = (x_4, y_3, z_3)$
$P_{23} = (x_3, y_4, z_3)$; $P_{24} = (x_4, y_4, z_3)$
$P_{25} = (x_3, y_3, z_4)$; $P_{26} = (x_4, y_3, z_4)$
$P_{27} = (x_3, y_4, z_4)$; $P_{28} = (x_4, y_4, z_4)$

$$\mathcal{I}_{p-v}^{(o_2)} = \sum_{k=3}^{4}\sum_{m=3}^{4}\sum_{n=3}^{4}\sum_{h=1}^{8}(-1)^{(k+m+n+1)}\gamma_h$$

$$\gamma_1 = -1/(12)s_z^4 \arctan\left(\frac{s_x s_y}{s_z R}\right)$$

$$\gamma_2 = -1/(12)s_y^4 \arctan\left(\frac{s_x s_z}{s_y R}\right) \quad ; \quad \gamma_3 = -1/(12)s_x^4 \arctan\left(\frac{s_y s_z}{s_x R}\right)$$

$$\gamma_4 = 1/6 s_y s_z \left(s_y^2 + s_z^2\right)\log\left(s_x + R\right) \quad ; \quad \gamma_5 = 1/12\left(s_z^4 - s_y^4\right)\arctan\left(s_y/s_z\right)$$

$$\gamma_6 = 1/6 s_x s_z \left(s_x^2 + s_z^2\right)\log\left(s_y + R\right) \quad ; \quad \gamma_7 = 1/6 s_x s_y \left(s_x^2 + s_y^2\right)\log\left(s_z + R\right)$$

$$\gamma_8 = -1/(18)\left(5/2 s_y^3 s_z + s_x s_z^3 - 5/2 s_y s_z^3\right) + 1/4 s_x s_y s_z R$$

$$\mathcal{I}_{p-v}^{(o_3)} = \sum_{k=3}^{4}\sum_{m=3}^{4}\sum_{n=3}^{4}(-1)^{(k+m+n+1)}\left[1/3 s_x s_y s_z (s_x^2 + s_y^2 + s_z^2)\right]$$

where $s_x = x_1 - x_k,\ s_y = y_1 - y_m,\ s_z = z_1 - z_n$ and $R = \sqrt{s_x^2 + s_y^2 + s_z^2}$

(a)

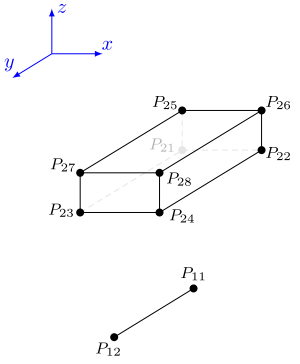

$P_{11} = (x_1, y_1, z_1)$; $P_{12} = (x_1, y_2, z_1)$
$P_{21} = (x_3, y_3, z_3)$; $P_{22} = (x_4, y_3, z_3)$
$P_{23} = (x_3, y_4, z_3)$; $P_{24} = (x_4, y_4, z_3)$
$P_{25} = (x_3, y_3, z_4)$; $P_{26} = (x_4, y_3, z_4)$
$P_{27} = (x_3, y_4, z_4)$; $P_{28} = (x_4, y_4, z_4)$

$$\mathcal{I}_{\ell-v}^{(o_2)} = \sum_{j=1}^{2}\sum_{k=3}^{4}\sum_{m=3}^{4}\sum_{n=3}^{4}(-1)^{(j+k+n+m+1)}\gamma_h$$

$$\gamma_1 = -1/(12)s_y s_z^4 \arctan\left(\frac{s_x s_y}{s_z R}\right) \quad ; \quad \gamma_2 = -1/60 s_y^5 \arctan\left(\frac{s_x s_z}{s_y R}\right)$$

$$\gamma_3 = -1/(12)s_x^4 s_y \arctan\left(\frac{s_y s_z}{s_x R}\right) \quad ; \quad \gamma_4 = 1/6 s_x s_y s_z \left(s_x^2 + s_z^2\right)\log\left(s_y + R\right)$$

$$\gamma_5 = 1/4 s_z\left[1/6 s_y^4 + 1/3 s_y^2 s_z^2 - 1/(10)s_z^4\right]\log\left(s_x + R\right)$$

$$\gamma_6 = 1/4 s_x\left[1/6 s_y^4 + 1/3 s_x^2 s_y^2 - 1/(10)s_x^4\right]\log\left(s_z + R\right)$$

$$\gamma_7 = -1/(240)s_y^4\left[s_y^4(s_x + s_z) + s_x^5 + s_z^5\right] + 1/(40)s_y^2(s_x^3 + s_z^3 + 4 s_x s_z R)$$

$$\gamma_8 = 7/(120)s_x s_z(s_x^2 - s_z^2)R + 1/(120)s_y(3 s_x^5 s_z + 14 s_x^3 s_z^3 + 3 s_x s_z^5)/(s_x^2 + s_z^2)$$

$$\mathcal{I}_{\ell-v}^{(o_3)} = \sum_{j=1}^{2}\sum_{k=3}^{4}\sum_{m=3}^{4}\sum_{n=3}^{4}(-1)^{(j+k+n+m+1)}\gamma$$

$$\gamma = 1/(12)s_x s_y^2 s_z\left[s_y^2 + 2(s_x^2 + s_z^2)\right]$$

where $s_x = x_1 - x_k,\ s_y = y_j - y_m,\ s_z = z_1 - z_n$ and $R = \sqrt{s_x^2 + s_y^2 + s_z^2}$

(b)

Fig. 14. Analytical formulas for point–volume $\mathcal{I}_{p-v}^{(o_2)}$ and $\mathcal{I}_{p-v}^{(o_3)}$ and line–volume $\mathcal{I}_{\ell-v}^{(o_2)}$ and $\mathcal{I}_{\ell-v}^{(o_3)}$ integrals, where $y_1 < y_2$, $x_3 < x_4$, $y_3 < y_4$, and $z_3 < z_4$. (a) Analytical formulas for the point–volume integrals. (b) Analytical formulas for the line–volume integrals.

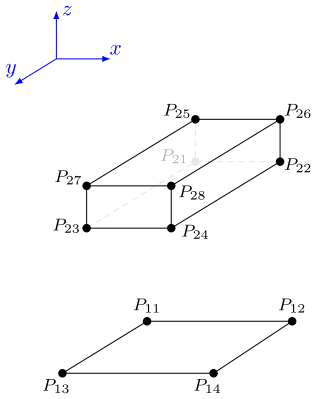

$P_{11} = (x_1, y_1, z_1)$; $P_{12} = (x_2, y_1, z_1)$
$P_{13} = (x_1, y_2, z_1)$; $P_{14} = (x_2, y_2, z_1)$
$P_{21} = (x_3, y_3, z_3)$; $P_{22} = (x_4, y_3, z_3)$
$P_{23} = (x_3, y_4, z_3)$; $P_{24} = (x_4, y_4, z_3)$
$P_{25} = (x_3, y_3, z_4)$; $P_{26} = (x_4, y_3, z_4)$
$P_{27} = (x_3, y_4, z_4)$; $P_{28} = (x_4, y_4, z_4)$

$$\mathcal{I}_{s-v}^{(o_2)} = \sum_{i=1}^{2}\sum_{j=1}^{2}\sum_{k=3}^{4}\sum_{m=3}^{4}\sum_{n=3}^{4}\sum_{h=1}^{8}(-1)^{(i+j+k+m+n)}\gamma_h$$

$$\gamma_1 = -1/(12)s_x s_y s_z^4 \arctan\left(\frac{s_x s_y}{s_z R}\right) \quad ; \quad \gamma_2 = -1/60 s_x s_y^5 \arctan\left(\frac{s_x s_z}{s_y R}\right)$$

$$\gamma_3 = -1/(60)s_x^5 s_y \arctan\left(\frac{s_y s_z}{s_x R}\right)$$

$$\gamma_4 = 1/4 s_x s_z\left[1/3 s_y^2(1/2 s_y^2 + s_z^2) - 1/(10)s_z^4\right]\log\left(s_x + R\right)$$

$$\gamma_5 = 1/4 s_y s_z\left[1/3 s_x^2(1/2 s_x^2 + s_z^2) - 1/(10)s_z^4\right]\log\left(s_y + R\right)$$

$$\gamma_6 = 1/(48)\left[s_x^2 s_y^2(s_x^2 + s_y^2) - 1/5(s_x^6 + s_y^6)\right]\log\left(s_z + R\right)$$

$$\gamma_7 = -1/(240)s_z\left[s_x s_y(s_x^3 + s_y^3) + (s_x + s_y)s_z^4\right] + 1/(40)s_x s_y(s_x + s_y)s_z^3$$

$$\gamma_8 = \left[1/(90)s_z^4 - 1/(80)(s_x^4 + s_y^4) + 1/(24)s_x^2 s_y^2 - 1/(45)(s_x^2 + s_y^2)s_z^2\right]s_z R$$

$$\mathcal{I}_{s-v}^{(o_3)} = \sum_{i=1}^{2}\sum_{j=1}^{2}\sum_{k=3}^{4}\sum_{m=3}^{4}\sum_{n=3}^{4}\sum_{h=1}^{8}(-1)^{(i+j+k+m+n)}\gamma$$

$$\gamma = 1/(24)s_x^2 s_y^2 s_z\left[s_x^2 + s_y^2 + 2s_z^2\right]$$

where $s_x = x_i - x_k,\ s_y = y_j - y_m,\ s_z = z_1 - z_n$ and $R = \sqrt{s_x^2 + s_y^2 + s_z^2}$

Fig. 15. Analytical formulas for the surface–volume integrals $\mathcal{I}_{s-v}^{(o_2)}$ and $\mathcal{I}_{s-v}^{(o_3)}$, where $x_1 < x_2$, $y_1 < y_2$, $x_3 < x_4$, $y_3 < y_4$, and $z_3 < z_4$.

REFERENCES

[1] K. S. Yee, "Numerical solution of initial boundary value problems involving Maxwell's equations in isotropic media," *IEEE Trans. Antennas Propag.*, vol. AP-14, no. 5, pp. 302–307, May 1966.

[2] J. M. Jin, *The Finite Element Method in Electromagnetics*, 3rd ed. Hoboken, NJ, USA: Wiley/IEEE Press, 2014.

[3] R. F. Harrington, *Field Computation by Moment Methods*. Malabar, FL, USA: Krieger, 1982.

[4] A. E. Ruehli, "Inductance calculations in a complex integrated circuit environment," *IBM J. Res. Dev.*, vol. 16, no. 5, pp. 470–481, Sep. 1972.

[5] A. E. Ruehli and P. A. Brennan, "Efficient capacitance calculations for three-dimensional multiconductor systems," *IEEE Trans. Microw. Theory Techn.*, vol. MTT-21, no. 2, pp. 76–82, Feb. 1973.

[6] A. E. Ruehli, "Equivalent circuit models for three dimensional multiconductor systems," *IEEE Trans. Microw. Theory Techn.*, vol. MTT-22, no. 3, pp. 216–221, Mar. 1974.

[7] A. E. Ruehli, G. Antonini, and L. Jiang, *Circuit Oriented Electromagnetic Modeling Using the PEEC Techniques*. Hoboken, NJ, USA: Wiley/IEEE Press, 2017.

[8] I. Kovacevic-Badstuebner, D. Romano, L. Lombardi, U. Grossner, J. Ekman, and G. Antonini, "Accurate calculation of partial inductances for the orthogonal PEEC formulation," *IEEE Trans. Electromagn. Compat.*, vol. 63, no. 1, pp. 82–92, Feb. 2021.

[9] L. Lombardi, G. Antonini, and A. E. Ruehli, "Analytical evaluation of partial elements using a retarded taylor series expansion of the Green's function," *IEEE Trans. Microw. Theory Techn.*, vol. 66, no. 5, pp. 2116–2127, May 2018.

[10] C. Hoer and C. Love, "Exact inductance equations for rectangular conductors with applications to more complicated geometries," *J. Res. Nat. Bur. Standards—C. Eng. Instrum.*, vol. 69, no. C, pp. 127–137, 1965.

[11] D. Romano, I. Kovacevic-Badstuebner, G. Antonini, and U. Grossner, "Efficient PEEC iterative solver for power electronic applications," *IEEE Trans. Electromagn. Compat.*, vol. 65, no. 2, pp. 546–554, Apr. 2023.

[12] R. Torchio, F. Lucchini, J.-L. Schanen, O. Chadebec, and G. Meunier, "FFT-PEEC: A fast tool from cad to power electronics simulations," *IEEE Trans. Power Electron.*, vol. 37, no. 1, pp. 700–713, Jan. 2022.

[13] M. Wang, C. Qian, J. K. White, and A. C. Yucel, "VoxCap: FFT-accelerated and tucker-enhanced capacitance extraction simulator for voxelized structures," *IEEE Trans. Microw. Theory Techn.*, vol. 68, no. 12, pp. 5154–5168, Dec. 2020.

[14] C. Qian and A. C. Yucel, "On the compression of translation operator tensors in FMM-FFT-accelerated SIE simulators via tensor decompositions," *IEEE Trans. Antennas Propag.*, vol. 69, no. 6, pp. 3359–3370, Jun. 2021.

[15] *MATLAB, version 9.11.0.1873467 (R2021b)*, The MathWorks Inc., Natick, MA, USA, 2021.

[16] G. Zhong and C.-K. Koh, "Exact closed-form formula for partial mutual inductances of rectangular conductors," *IEEE Trans. Circuits Syst. I, Fundam. Theory Appl.*, vol. 50, no. 10, pp. 1349–1352, Oct. 2003.

[17] Z. Song, F. Duval, D. Su, and A. Louis, "Stable partial inductance calculation for partial element equivalent circuit modeling," *Appl. Comput. Electromagn. Soc. J.*, vol. 25, no. 9, pp. 738–749, 2010.

[18] D. P. Laurie, "Calculation of Gauss-Kronrod quadrature rules," *Math. Comput.*, vol. 66, no. 219, pp. 1133–1145, Jul. 1997.

Daniele Romano was born in Campobasso, Italy, in 1984. He received the Laurea degree in computer science and automation engineering and the Ph.D. degree in industrial engineering from the University of L'Aquila, L'Aquila, Italy, in 2012 and 2018, respectively.

Since 2012, he has been with the UAq EMC Laboratory, University of L'Aquila, where he is currently a Researcher. His research interests include electromagnetic compatibility (EMC) modeling and analysis, algorithm engineering, and speedup techniques applied to EMC problems.

Ivana Kovacevic-Badstuebner (Senior Member, IEEE) received the Ph.D. degree in electrical engineering from ETH Zürich, Zürich, Switzerland, in 2012.

From 2008 to 2015, she was with the Power Electronics Systems Laboratory, ETH Zürich, where she focused on the prediction of electromagnetic behavior of power electronics systems based on the developed numerical techniques and the lifetime modeling of power semiconductor modules. In March 2016, she joined the Advanced Power Semiconductor Laboratory, ETH Zürich. Her research interests include novel packaging technologies for SiC power devices, the optimization of power module layout with respect to electromagnetic interference, and multidomain modeling of power semiconductor devices and their modules.

Ulrike Grossner (Member, IEEE) received the Dipl.-Phys. and Dr.rer.nat. degrees from Friedrich-Schiller-University Jena, Jena, Germany, in 1997 and 2000, respectively.

In 2014, she became a Full Professor with ETH Zürich, Zürich, Switzerland, where she established the Advanced Power Semiconductor Laboratory, working on devices and packaging for advanced power semiconductors.

Giulio Antonini (Senior Member, IEEE) received the Laurea degree (*cum laude*) from the University of L'Aquila, L'Aquila, Italy, in 1994, and the Ph.D. degree from the University of Rome "La Sapienza," Rome, Italy, in 1998, both in electrical engineering.

Since 1998, he has been with the UAq EMC Laboratory, University of L'Aquila, where he is currently a Professor. He has authored more than 300 papers in international journals and conferences. He has coauthored the book titled *Circuit Oriented Electromagnetic Modeling Using the PEEC Techniques* (Hoboken, NJ, USA: Wiley/IEEE Press, 2017). His research interests include computational electromagnetics.

Open Access funding provided by 'Università degli Studi dell'Aquila' within the CRUI CARE Agreement